Received: 18 April 2019 | Revised: 5 October 2019 | Accepted: 15 November 2019

DOI: 10.1002/qj.3708

Quarterly Journal of the Royal Meteorological Society RMetS

RESEARCH ARTICLE

Tropical atmospheric drivers of wintertime European precipitation events

Ronald K. K. Li[1] | Tim Woollings[1] | Chris O'Reilly[1] | Adam A. Scaife[2,3]

[1]Atmospheric, Oceanic and Planetary Physics, University of Oxford, Oxford, UK

[2]Hadley Centre, Met Office, Exeter, UK

[3]College of Engineering, Mathematics and Physical Sciences, Exeter University, Exeter, UK

Correspondence
R. Li, Atmospheric, Oceanic and Planetary Physics, University of Oxford, Sherrington Road, Oxford OX1 3PU, UK
Email: ronald.li@physics.ox.ac.uk

Funding information
NERC IMPETUS project NERC SummerTIME project the Joint UK BEIS/DEFRA Met Office Hadley Centre Climate Program, NE/L01047X/1, NE/M005887/1, GA01101

Abstract

From observations, we identify a wave-like pattern associated with northwestern European seasonal precipitation events. These events are associated with tropical precipitation anomalies, prompting us to investigate if there are any tropical–extratropical teleconnections, in particular the role of tropical anomalies in driving extratropical dynamics through Rossby wave propagation. Using a hierarchy of models from ray tracing to barotropic and baroclinic models, we investigate the Rossby wave mechanism and test potential tropical drivers and yield qualitative results. Using a barotropic model, we identify potential Rossby wave source regions which are consistent between the observations and the model. These regions include the tropical western and eastern Atlantic, the subtropical eastern Atlantic and, to a smaller degree, the subtropical eastern Pacific. Zonal wavenumber 2 and 3 components of the barotropic model responses match well with the observations and ray tracing supports the importance of these components. We use a baroclinic model to investigate the link between the observed Rossby wave source anomalies and the observed tropical precipitation anomalies. The reduced precipitation observed in the tropical Atlantic just north of the Equator can generate some of the observed Rossby wave source anomalies in the tropical Atlantic, while the increased precipitation observed in the tropical eastern Pacific can generate some of the observed Rossby wave source anomalies in the subtropical eastern Pacific. Our results can also be applied to European drought events because of the qualitative linearity in the observations and in our linear methods.

KEYWORDS

drought, European climate, idealised models, precipitation, Rossby wave, teleconnection, tropical rainfall

1 | INTRODUCTION

Many studies have looked at recent wet European winters. Scaife *et al.* (2017a) showed that seasonal forecasts of the wet UK and northwestern Europe in the early winter of December 2015 were likely driven by the extreme El Niño of that winter. Knight *et al.* (2017) found that the extratropical pattern associated with the record UK

rainfall of winter 2013–2014 could be partly reproduced by relaxing models especially over the tropical Atlantic, and suggested that enhanced Amazonian convection could be an atmospheric driver of the extratropical Rossby wave. Their analysis might suggest similar atmospheric drivers contributing to extreme precipitation events across neighbouring regions in the North Atlantic–European sector.

The Quasi-Biennial Oscillation (QBO) also appears to have contributed to the extreme conditions in 2013–2014 (Huntingford *et al.*, 2014; Knight *et al.*, 2017). The tropical stratospheric signal propagates poleward then downward to affect the North Atlantic surface climate (Anstey and Shepherd, 2014), and is consistent with a strong Atlantic jet stream in that winter. Studies have found predictability in the QBO (Scaife *et al.*, 2014b) and in its northern winter teleconnection on seasonal time-scales(O'Reilly *et al.*, 2019).

The North Atlantic Oscillation (NAO) is a major source of seasonal variability in the North Atlantic–European region. Many potential sources of skill in NAO prediction have been suggested (Smith *et al.*, 2016). The NAO is a phenomenon arising from midlatitude eddy–mean flow interaction, but can be triggered by Rossby waves propagating from the Tropics (Feldstein, 2003). Scaife *et al.* (2014a) showed skilful seasonal prediction of the wintertime NAO, and Scaife *et al.* (2017b) showed that tropical rainfall explained 40% of the variance in the seasonal forecast of the NAO through Rossby waves. Tropical sea surface temperatures are also found to affect the NAO (Davini *et al.*, 2015). Manola *et al.* (2013) showed that tropical forcings can account for 14% and 35% of the wind variance associated with the positive and negative NAO respectively, indicating a pronounced impact of tropical forcing on the NAO.

While not many studies have looked at European dry winters, Dunstone *et al.* (2018) looked at the recently very dry European winter of 2016–2017. They found evidence for a Rossby wave triggered by anomalous tropical Atlantic precipitation and propagating into Europe. Instead of investigating individual European wet and dry winters, we investigate these events together. As we will show, the seasonal anomalies between European dry and wet winters show qualitative linearity. This motivates us to look at dry and wet winters together in a linear framework. We focus on the influence of stationary propagating Rossby waves in the troposphere from the Tropics and Subtropics, using a hierarchy of models from ray tracing, barotropic model to baroclinic model. We emphasize that we do not expect Rossby wave propagation from the Tropics into the Extratropics to be the only mechanism for these events. However, there is evidence that recurring low-frequency atmospheric circulation anomalies organize storm track anomalies (Branstator, 1995), and these low-frequency anomalies are strongly driven by the Tropics. Here our aim is not to quantitatively reproduce the observed anomalies, but to test the mechanisms of tropical influence in idealised models with a restricted number of processes.

2 | METHODS

2.1 | Barotropic model

The barotropic model (O'Reilly *et al.*, 2018) is based on Hoskins and Ambrizzi (1993). It integrates the damped barotropic vorticity equation.

Without any forcing, the basic state is maintained by the inverse initial tendency. The forcing is specified as a Rossby wave source (RWS) and all of our experiments apply a forcing which is constant in time. The RWS is calculated using the expression from Sardeshmukh and Hoskins (1988),

$$\mathrm{RWS} = -\nabla \cdot (\mathbf{V}_\chi \zeta) = -\mathbf{V}_\chi \cdot \nabla\zeta - \zeta\nabla \cdot \mathbf{V}_\chi, \qquad (1)$$

where the first term on the right is the vorticity advection by the divergent wind and the second term is the vortex stretching.

We multiply the RWS by 10^{-6} to make the calculation effectively linear (Hoskins and Ambrizzi, 1993), and the model response is scaled back up by 10^6. Scaling down the forcing effectively makes the nonlinear terms negligible. This allows us to look at the most basic, linear wave propagation without nonlinear complications, for example the wave interacting with itself. However, our results are found to be similar without scaling down the RWS. We use the climatological basic states on 250 hPa from the NCEP DOE Reanalysis 2 (Kanamitsu *et al.*, 2002). This set-up allows us to investigate the propagation of stationary Rossby waves from a tropical forcing that is stationary in time, on a basic state that is stationary in time. We present the quasi-stationary results averaged between days 7 and 10.

In the patch method, we run the experiment 544 times, with each forced by an idealised RWS patch resembling a Green's function. Similar to Barsugli and Sardeshmukh (2002), each patch has a 2D cosine-square form

$$P_k(\lambda,\phi) = A\cos^2\left(\frac{\pi}{2}\frac{\lambda-\lambda_k}{\lambda_w}\right)\cos^2\left(\frac{\pi}{2}\frac{\phi-\phi_k}{\phi_w}\right) \qquad (2)$$

within the rectangle spanned by $\lambda_k \pm \lambda_w$ in longitude and $\phi_k \pm \phi_w$ in latitude, where λ_k and ϕ_k specify the centre of each patch, and λ_w and ϕ_w are the half-widths in longitude and latitude respectively. Outside the rectangle,

P_k is set to zero everywhere. The advantage is that the distance between the centres of neighbouring patches equals the half-width of the cosine-square, so that a uniform plateau of forcing can be achieved upon addition of neighbouring patches. Each patch is around 11° wide zonally ($2 \times \lambda_w$) and 5° wide meridionally ($2 \times \phi_w$). Together they cover all longitudes with 32 patches, and cover latitudes from 45°S to 45°N with 17 patches, resulting in a total of 544 experiments. We do not include more poleward patches because we are interested in waves forced from the Tropics and the Subtropics. We use an amplitude A of $2{\times}10^{-11}\mathrm{s}^{-2}$, which, when combined with neighbouring patches, gives a uniform RWS amplitude similar to the observed anomalies. We remove the zonal mean forcing at each latitude before putting it into the barotropic model, because we are interested in the forcing of Rossby waves rather than zonal mean circulation anomalies.

While the observed teleconnections in this study are measured at interannual time-scale, our models operate at the daily time-scale. Our interpretation of the model results is that, while the triggered waves from the Tropics only take several days to propagate into the Extratropics, the persistency or the high frequency of occurrence of anomalous tropical forcings keeps triggering the stationary waves in most days of the season, which show up in the seasonal time-scale. While we specifically focus on seasonal anomalies, further examination of intraseasonal anomalies (e.g., Davies, 2015; Röthlisberger *et al.*, 2019) may provide complementary insights to our study.

2.2 | Ray tracing

We take the linear barotropic dispersion relation with no meridional basic flow. We use a 60° sectoral zonal averaging on the climatological 250 hPa zonal wind from NCEP2. The zonal averaging represents a typical wave scale (Scaife *et al.*, 2017a; Ayarzagüena *et al.*, 2018). We calculate the stationary wavenumber K_s at every gridpoint from this smoothed climatological wind (Hoskins and Karoly, 1981). To sample the sensitivity to the starting position of a ray, we also plot an ensemble of eight other rays located around a square of 5° in both longitude and latitude centred on the first ray.

2.3 | Baroclinic model

We use the Reading Intermediate Global Circulation Model version 1 (IGCM1; Hoskins and Simmons, 1975), with a T42 horizontal spectral truncation and 15 vertical levels. Similar to the barotropic experiments, we apply an inverse initial tendency forcing in all prognostic equations to maintain the basic state, in the absence of other forcing. We define the basic state using ERA-Interim (ERA-I; Dee *et al.*, 2011) reanalysis 1980–2017 December–January–February (DJF) climatology, but little difference is found between the basic states of ERA-I and NCEP2. Unlike specifying the RWS in the barotropic model, we specify heating in the baroclinic model (Hoskins and Karoly, 1981; Liu *et al.*, 2007). We use an elliptical heating on the horizontal tangent plane, with a sine-squared half-wave vertical structure between the surface and the tropopause, to give an upper-tropospheric peak at around 400 hPa. Our vertical heating structure follows those used in Jin and Hoskins (1995) and Matthews *et al.* (2004), which were shown to be consistent with analysed observational data. The heating is steady and is scaled by 10^{-6} to focus on linear stationary Rossby wave propagation, with the responses subsequently scaled back up by 10^6. However, results are again similar without scaling down the heating.

The observed vertically integrated heating is calculated based on a similar index to Li and Wettstein (2012), where the heating is dominated by tropical convection latent heating. We average the responses between days 10 and 14, similar to studies using the same model (Jin and Hoskins, 1995; Matthews *et al.*, 2004). This is longer than the 7–10 days for the wave to develop in the barotropic model. This is because, whereas the RWS is specified from day 0 in the barotropic model, it takes time for the baroclinic model to set up the RWS from the imposed heating.

2.4 | Significance testing

To evaluate the statistical significances of the linear regressions in Figures 1 and 2, we apply the F-test to calculate the p-values. To account for the multiple hypothesis tests across all the gridpoints, we control the false discovery rate (Wilks, 2016) by choosing α_{FDR} to be 0.10.

3 | OBSERVATIONAL ANALYSES

We first diagnose the atmospheric dynamics associated with European precipitation events in DJF using the ERA-20C reanalysis (Poli *et al.*, 2016) available for the whole Twentieth Century. We use the Climatic Research Unit (CRU) land precipitation data (Harris *et al.*, 2014) to match the period from 1902 to 2010. Figure 1b shows our northwestern European box (0°E–20°E, 45°N–55°N). In addition to the CRU precipitation data which are only available over land, we also use the Global Precipitation Climatology Project (GPCP) combined surface precipitation data (Adler *et al.*, 2003). The advantage of

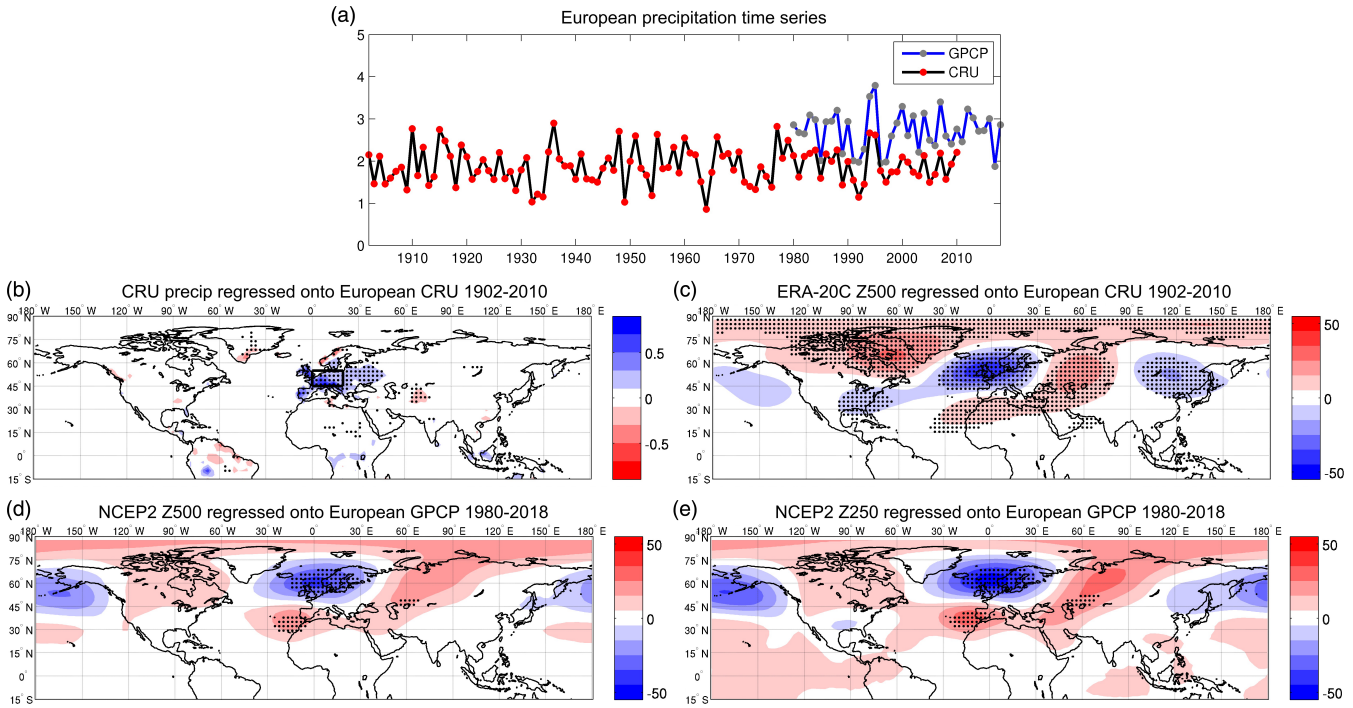

FIGURE 1 Northwest European precipitation time series and the robustness of the wave pattern. (a) Precipitation time series over our European box, using CRU (black) and GPCP (blue). (b) CRU precipitation regressed onto the CRU standardized European precipitation time series (mm·day^{-1}), with the black box indicating northwestern Europe. Black dots denote a significant linear regression relationship (Section 2.4). (c, d) 500 hPa geopotential heights regressed onto the CRU standardized European precipitation time series (m), and onto the GPCP standardized European precipitation time series (m). (e) is as (d), but for 250 hPa

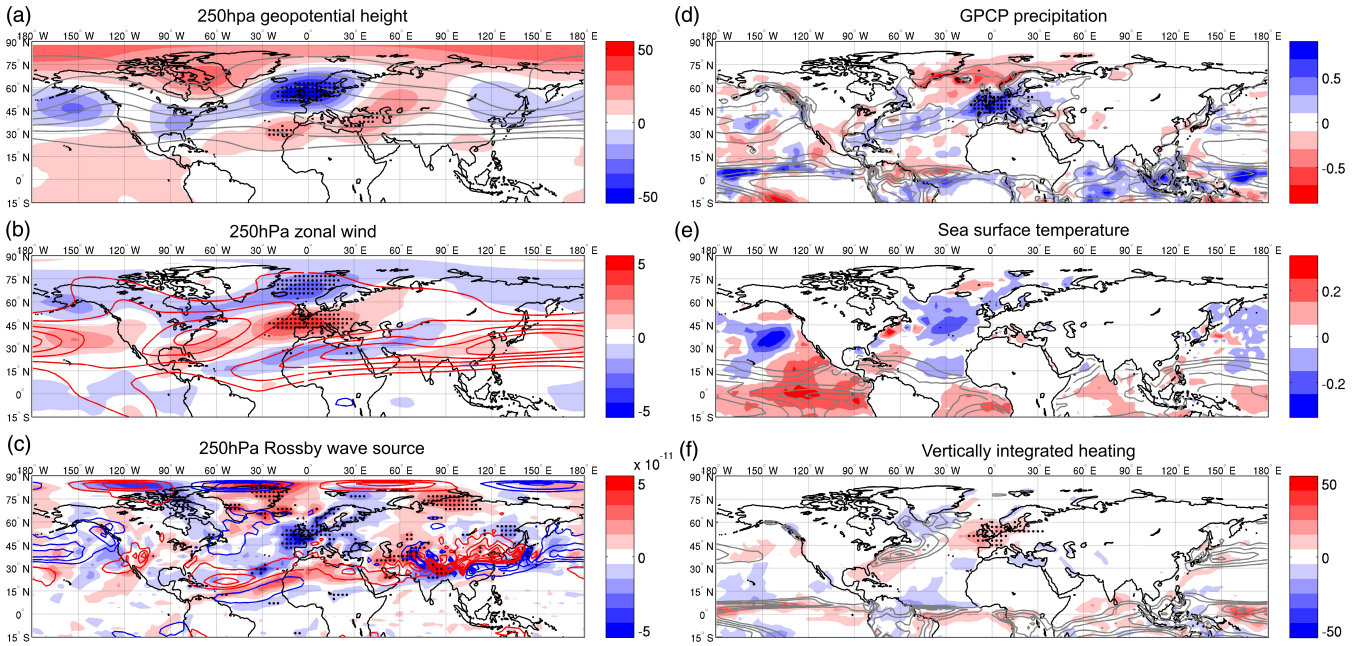

FIGURE 2 Anomalies associated with European precipitation events. Colour shading shows the regressions onto the standardized European region CRU precipitation time series between 1980 and 2010, for (a) geopotential height at 250 hPa (m), (b) zonal wind at 250 hPa (m·s^{-1}), (c) Rossby wave source at 250 hPa (s^{-2}), (d) GPCP precipitation (mm·day^{-1}), (e) sea surface temperature (C) and (f) vertically integrated heating (W·m^{-2}). Black dots denote a significant linear regression relationship (Section 2.4). Solid contours show the climatologies, with contour intervals (a) 200 from 9,600 m, (b) 10 from 10 m·s^{-1}, (c) 1×10^{-10} s^{-2} from zero with positive red and negative blue, and with zero omitted, (d) 2 from 2 mm·day^{-1}, (e) 1° from 25°C, and (f) 50 from 50 W·m^{-2}

these over CRU is that they combine satellite observations and therefore makes precipitation data available over the ocean. This is useful in the Tropics where precipitation over the oceans is important for extratropical teleconnections (Scaife *et al.*, 2017b; Scaife *et al.*, 2019). The disadvantage of GPCP is that it is only available for a shorter period of time than CRU. Figure 1a shows that the GPCP time series averaged over our European box correlates well with CRU over their overlapping period of 1980–2010 ($r = 0.84$, significant at 95% confidence), although GPCP is systematically wetter.

While much focus in the literature has been placed on the NAO teleconnections and associated precipitation, and also on the East Atlantic (EA) pattern to a lesser extent, not much focus has been placed on subsequent modes of variability. Therefore, we have chosen our region such that it has a weak projection onto the NAO and the EA precipitation. There is no significant trend in our CRU European precipitation in Figure 1a, so we do not detrend the precipitation data. The precipitation is more concentrated in the southern flank of our box (Figure 1b). It also shows that our European precipitation index is positively correlated with precipitation over the Iberian Peninsula, the UK, southern Sweden and western Russia, but anti-correlated with precipitation over Norway and southern Greenland. The above links still hold qualitatively with the twenty driest and twenty wettest seasonal composites, suggesting the precipitation and circulation show qualitative linearity. Instead of just focusing on the European precipitation events, we investigate both wet and dry seasons together.

To relate our European precipitation to the preferred patterns of large-scale atmospheric dynamics, we perform empirical orthogonal function (EOF) analysis (Hannachi *et al.*, 2007) on the ERA-20C 500 hPa geopotential height (Z500) over the North Atlantic–European region (90°W–90°E, 20°N–90°N). EOF1 is the NAO and EOF2 is the EA. Our northwestern European box precipitation time series correlates with NAO+ at −0.44 and with EA+ at 0.20, both significant at 95% confidence, suggesting these EOFs capture some but not the majority of the variability.

Figure 1c shows the 500 hPa geopotential height regressed onto the standardized European precipitation time series, for the period 1902 to 2010. It is suggestive of an extratropical wave linking areas of statistical significance, for example the higher heights over northeastern North America, lower heights over the UK, higher heights over western Asia and lower heights over eastern Asia. There are also significant anomalies in the Subtropics, with lower heights over southeastern North America and higher heights over northwestern Africa.

We also investigate the more recent period up to 2018. Since ERA-20C only spans the period 1902 to 2010, we make use of the NCEP2 dataset. The 500 hPa height regression using GPCP precipitation and NCEP2 heights for 1980 to 2018 shows similar anomalies across North America, the UK, western Asia and north Africa (Figure 1d), but the significance is less robust for this more recent shorter period. The 250 hPa height regression shows an equivalent barotropic structure (Figure 1e). For the rest of our study, we focus on the overlapping period of 1980 to 2010 from Figure 1a.

Figure 2a shows the NCEP2 250 hPa heights regressed onto the standardized European region CRU precipitation time series from 1980 to 2010. It is very similar to the ERA-20C 500 hPa height regression in Figure 1c from 1902 to 2010. The zonal wind shows an extension in the North Atlantic jet exit and a poleward shift in the Asian jet entrance (Figure 2b). This reflects the aforementioned partial correlation with the NAO. Figure 2c shows the 250 hPa RWS regression, calculated from the horizontal winds. There are statistically significant RWS anomalies in the tropical Atlantic below 15°N. Wet and dry composites for both Z250 and RWS show qualitative linearity of these anomalies. Although the RWS has a quadratic form, Hardiman *et al.* (2019) also showed linearity in the RWS, to different ENSO strengths.

Figure 2d shows the GPCP precipitation regression. In the tropical Atlantic, the Intertropical Convergence Zone (ITCZ) shifts southward when European precipitation is high. The reduced precipitation just north of the Equator is also observed on land in northeastern South America in the longer period of 1902 to 2010 in Figure 1. The relationship between the increased precipitation in the tropical Atlantic just south of the Equator and the positive region of RWS along 15°N from 60°W to 30°W in Figure 2c has also been reported in a seasonal forecast model study (Scaife *et al.*, 2017b, their figure 7d). The tropical Pacific ITCZ also strengthens when European precipitation is high. Since different precipitation datasets may show inconsistent estimates (Sun *et al.*, 2018), we repeat the precipitation regression in Figure 2d using another satellite-related precipitation product – the Climate Prediction Center (CPC) Merged Analysis of Precipitation (CMAP; Xie and Arkin, 1997) – as well as another global gauge-based product from the Global Precipitation Climatology Centre (GPCC; Schneider *et al.*, 2016). The southward shift of the tropical Atlantic ITCZ and the strengthening of the tropical Pacific ITCZ are also seen in CMAP, and the reduced precipitation on land in northeastern South America is also seen in both CMAP and GPCC (not shown). Related to the reduced precipitation just north of the Equator in the tropical Atlantic, upon closer inspection the Sahel also shows a slight reduction in precipitation. The Sahel has been linked to sea surface temperatures (SSTs) in the equatorial Atlantic (Folland *et al.*, 1986). Figure 2e shows higher SSTs in the equatorial Atlantic and lower SSTs further north,

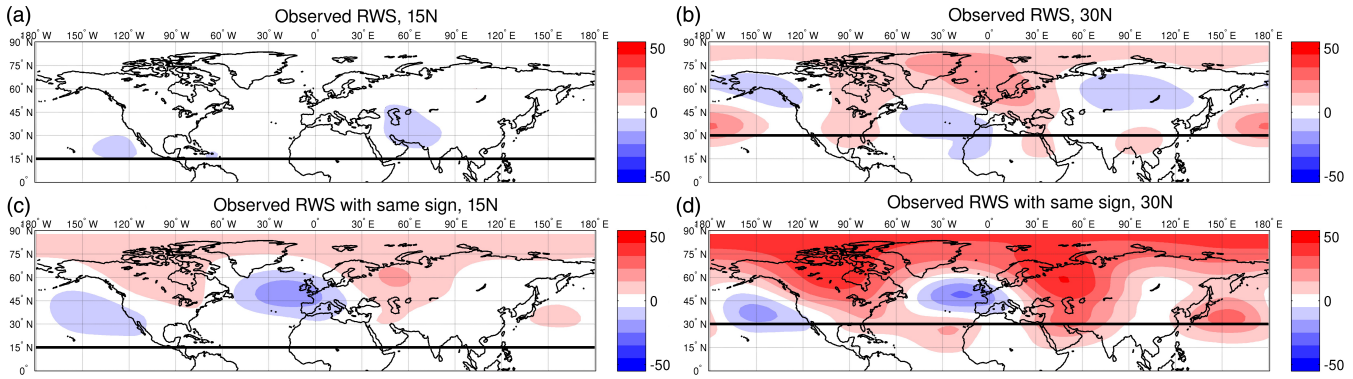

FIGURE 3 Barotropic model responses to observed forcings. 250 hPa geopotential height responses (m) from barotropic experiments, using (a, b) the observed Rossby wave source and (c, d) the observed Rossby wave source where the sign agrees with the linearly combined patches. Forcings up to 15°N are used in (a, c), and up to 30°N in (b, d)

consistent with Lamb (1978) who showed that a dry Sahel is associated with tropical Atlantic SST maximum locating south of its average position.

Figure 2f shows the vertically integrated heating, with a similar pattern in the Tropics to the GPCP precipitation because precipitation dominates the atmospheric heating in the Tropics. The precipitation of around 0.4 mm·day^{-1} in the tropical Atlantic in Figure 2d corresponds to around 10 W·m^{-2} of heating in Figure 2f.

To summarize, we have identified a large-scale wave pattern associated with seasonal European precipitation events, which is qualitatively linear with respect to the dry and wet events. We have also identified anomalous tropical precipitation via a southward shift in the tropical Atlantic, and to a smaller extent a strengthening in the tropical eastern Pacific. There are also statistically significant RWS anomalies in the tropical Atlantic. In the following sections, we drive waves from the Tropics in a barotropic and a baroclinic model, as well as using ray tracing, to investigate this teleconnection.

4 | BAROTROPIC MODEL EXPERIMENTS

4.1 | Global forcing

We force the barotropic model using the observed RWS anomalies isolated over the Tropics and the Subtropics from Figure 2c. Forcing with the 15°S–15°N observed RWS produces a very weak extratropical response (Figure 3a), while forcing over 30°S–30°N produces a stronger response (Figure 3b). However, both responses match poorly to the observed heights in Figure 2a. One possible reason is that the observed RWS is noisy. Therefore, simply forcing the model with all the observed RWS cannot reproduce the observations.

Next, we match the 250 hPa heights response of each of our patch experiments to the observed 250 hPa heights. For each of our 544 patch experiments (Section 2.1), we calculate a weighting by taking the dot product in the Extratropics between the 250 hPa response from each patch forcing and the observation, and standardize by dividing by the dot product of the observed pattern with itself. We then use this weighting to linearly combine all the patch experiments, to get the best-match response to the observed pattern achievable by the barotropic model, and the associated forcings needed to generate this best match. The metric for deciding the best match is therefore by maximising the area-weighted projection.

The linear combination of the patch experiments response (Figure 4a) is able to match the observations (Figure 2a) well, with lower heights over the UK, higher heights over western Russia, lower heights south of the Aleutian Islands and higher heights over the Hudson Bay. The residual shows a zonal pattern over southern and northern Europe (Figure 4b) which the patch experiments cannot capture. This north–south height difference partly projects onto the NAO, which is consistent with the aforementioned partial temporal correlation between our European precipitation and the NAO index. The NAO is well-known to be forced by extratropical eddy activity, and thus is not expected to be captured by the Rossby wave mechanism in the patch experiments.

Forcings that can generate the best match to the observed heights in this model show a northwest–southeast tilted banded structure over the Tropics and the Subtropics (Figure 4c), with strongest signals in the eastern Pacific and the Atlantic. This tilt is consistent with the phase tilt of Rossby waves propagating northeastward from the Tropics into the Extratropics. To identify potential forcing regions that are consistent between the observed RWS and the model, we compare the linearly combined patches (Figure 4c) to the observed

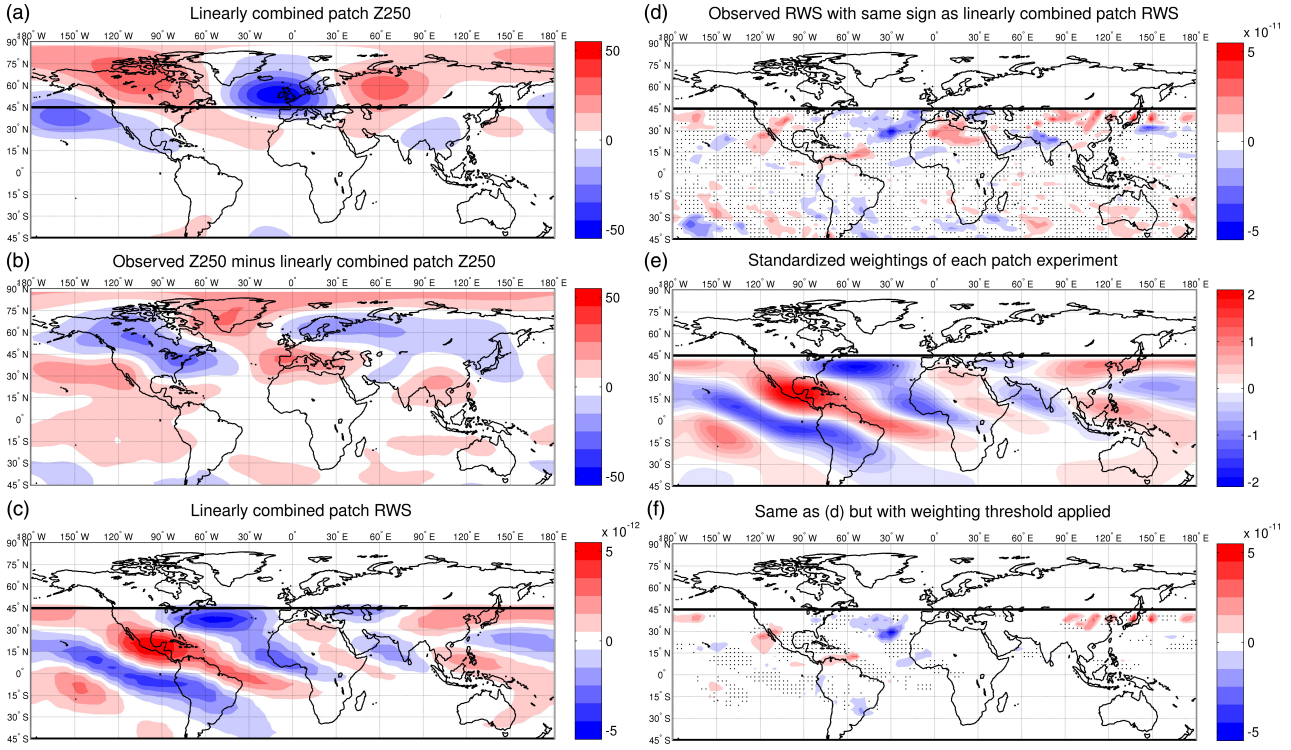

FIGURE 4 Barotropic model patch method results. (a) Best match in 250 hPa geopotential height (m) from the barotropic model patch experiments to the observation. Black lines indicate the patch forcings region. (b) Observed 250 hPa heights minus (a) (m). (c) Linearly combined Rossby wave source from patch experiments (s^{-2}). (d) Regions of observed Rossby wave source that are the same sign as the linearly combined patches (s^{-2}). Regions where the signs do not agree are set to zero and are dotted. (e) Standardized weightings of each patch experiment. (f) is as (d), but with a weighting threshold applied to filter out small weightings

RWS (Figure 2c) to isolate regions where both agree in the sign of the RWS.

There are some similarities between the observed RWS and the linearly combined patches (red and blue in Figure 4d). However, there are also many regions where the observed RWS is of the opposite sign to the linearly combined patches (black dots in Figure 4d). While this means that in these many regions the observed RWS generates a response in the model with a negative projection onto the observed wave, many of these projections are only very weakly negative. Figure 4e shows the standardized weighting of each patch experiment, which is similar to the linearly combined patch RWS in Figure 4c. To focus on regions where the standardized weighting is large, we apply a weighting threshold in Figure 4d to produce Figure 4f. As the maximum absolute value of the weightings in Figure 4e is around 2, we can choose any threshold less than 2 in absolute value and define large weightings as having an absolute value above this threshold, and define a weighting as small otherwise. Figure 4f shows results with a threshold of 0.6 chosen, which is around one-third of the maximum weighting. The red and blue regions show the observed RWSs that agree in sign with the linearly combined patches and with large weightings, the black dotted regions show the observed RWS that do not agree in sign with the linearly combined patches and with large weightings, and the white regions show the remaining small weightings with the observed RWS either agreeing or disagreeing in sign with the linearly combined patches. The main results are also not too sensitive to choosing a more loose threshold of 0.5 or a more strict threshold of 0.7 (not shown).

Compared to the original in Figure 4d, a lot of the black dotted regions have been filtered out. As the threshold is applied as an absolute value to act on both positive and negative weightings, some of the red and blue regions in Figure 4d are also filtered out. Still, there are several large regions remaining in Figure 4f where the observed RWSs have the same sign as the patches. In the Tropics up to 15°N, these include the positive source in the tropical western Atlantic and the negative source in the tropical eastern Atlantic. In the Subtropics above 15°N, these include the positive source in the subtropical eastern Pacific over the Gulf of California and the negative source in the subtropical eastern Atlantic.

Next, we force the model with the RWS in Figure 4f where we have set the RWS to zero over regions where the sign of the observed RWS disagrees with the sign of the linearly combined patches (the black dots). The responses from forcing with 15°S–15°N and 30°S–30°N in Figure 4f

are shown in Figures 3c,d respectively. By construction, the response from each RWS in Figure 4c has a reasonable projection onto the observed heights, therefore each RWS in Figure 4c gives a response more or less similar to Figure 4a. As the RWSs in Figure 4f are a subset of the RWSs in Figure 4c, it is not too surprising that the response from Figure 4f (as shown in Figure 3c,d) resembles the response from Figure 4c (as shown in Figure 4a). Compared with the responses using all the observed RWSs as forcings (Figure 3a,b), the responses in Figures 3(c,d) using the RWSs from Figure 4f match the observed heights quite well.

Finally, we discuss the large regions in the tropical eastern Pacific and tropical Atlantic where the observed RWS has an opposite sign to the linearly combined patches, and which also produces heights with strong negative projections onto the observed heights (black dots in Figure 4f). A possible reason is that some of these observed anomalies are consequences of the large-scale circulation anomalies, which could be coming from the Walker circulations or from the extratropical waves. The extratropical waves can generate anomalous vorticities and divergent winds, which can propagate back into the Tropics and affect the observed tropical RWS nonlinearly. A second possibility is that the observed RWS is obtained from regression, which does not imply causality. Other atmospheric processes that are correlated with our European precipitation time series are captured in the regression, which may just be noise. In the baroclinic model section, we will investigate the association of the RWS with tropical heating. However, further investigations into whether some of the observed RWSs are feedbacks or are noise are beyond our study.

4.2 | Individual patches

To further investigate the importance of the tropical and subtropical RWSs in the Atlantic and the Pacific, Figure 5 shows the responses from individual RWS patches selected from Figure 4f where the observed RWS and the linearly combined patches are consistent. The four idealised patches include the tropical western Atlantic, the tropical eastern Atlantic, the subtropical eastern Atlantic and the subtropical eastern Pacific. The amplitudes are chosen to match the observed amplitudes in Figure 4f. For example, area-averaging over the 2D cosine-squared patch in the tropical western Atlantic gives an average amplitude of 2×10^{-11} s^{-2}, which matches the observation.

Figure 5a shows a wave emanating from the patch in the tropical western Atlantic, crossing the North Atlantic into Europe and Scandinavia. Although this response captures the lower heights over our European box, it does not capture the higher heights downstream in western Russia or upstream in Baffin Bay. Figure 5b shows a wave emanating from the patch in the tropical eastern Atlantic. It crosses the Mediterranean Sea into western Russia. In addition to capturing the lower heights over Europe, this response captures the downstream higher heights over western Russia. Combining both patches (Figure 5e) gives a pattern more similar to the observation than from each patch individually. This suggests that, when considering RWSs below 15°N, these two patches in the tropical Atlantic can together contribute to the observed pattern over Europe and western Russia. There is another region of large-amplitude RWS in the subtropical eastern Atlantic. The response from this patch (Figure 5c) is similar to that of the previous two patches within 15°N. This suggests that this patch at higher latitude can reinforce the response of the patches at lower latitude in the tropical Atlantic, even if it is a secondary source stimulated by the tropical sources.

In the subtropical eastern Pacific, Figure 5d shows a wave propagating from the Gulf of California across North America into the North Atlantic but this makes only a small contribution. It captures the lower heights over Europe and the higher heights in northwestern Russia and northern Canada. This response is weaker than the combined responses from the three Atlantic forcings in Figure 5f which reproduces most of the observed pattern and amplitude. It resembles Figure 3d and shows that our Atlantic patches already capture most of the important same-sign RWSs in Figure 4f. The response of lower heights over the UK also has an amplitude which matches closely that of the observation. To summarize, RWS anomalies in the tropical Atlantic (lower than 15°N) can trigger the observed extratropical wave. Anomalies in the subtropical Atlantic (between 15°N and 30°N) can enhance the wave, and the subtropical Pacific RWS anomaly appears to make a small additional contribution (Figure 5g). However, some of these subtropical RWS anomalies are likely to be part of the wave itself.

As the observed pattern is quite zonal, we analyze the contribution from each zonal wavenumber (k) of its decomposition. Also, Fourier decomposition allows us to compare with the ray tracing results later, which are performed for each wavenumber separately. Figure 6 shows the $k2$ and $k3$ components of the observed pattern, and of the barotropic model responses to individual patches from Figure 5. Only $k2$ and $k3$ are shown because these are found to be the dominant components in midlatitudes, in agreement with Scaife *et al.* (2017b).

The barotropic model with patches in the tropical western Atlantic (Figure 6c,d) and the subtropical eastern Atlantic (Figure 6g,h) produce very similar $k2$ and $k3$

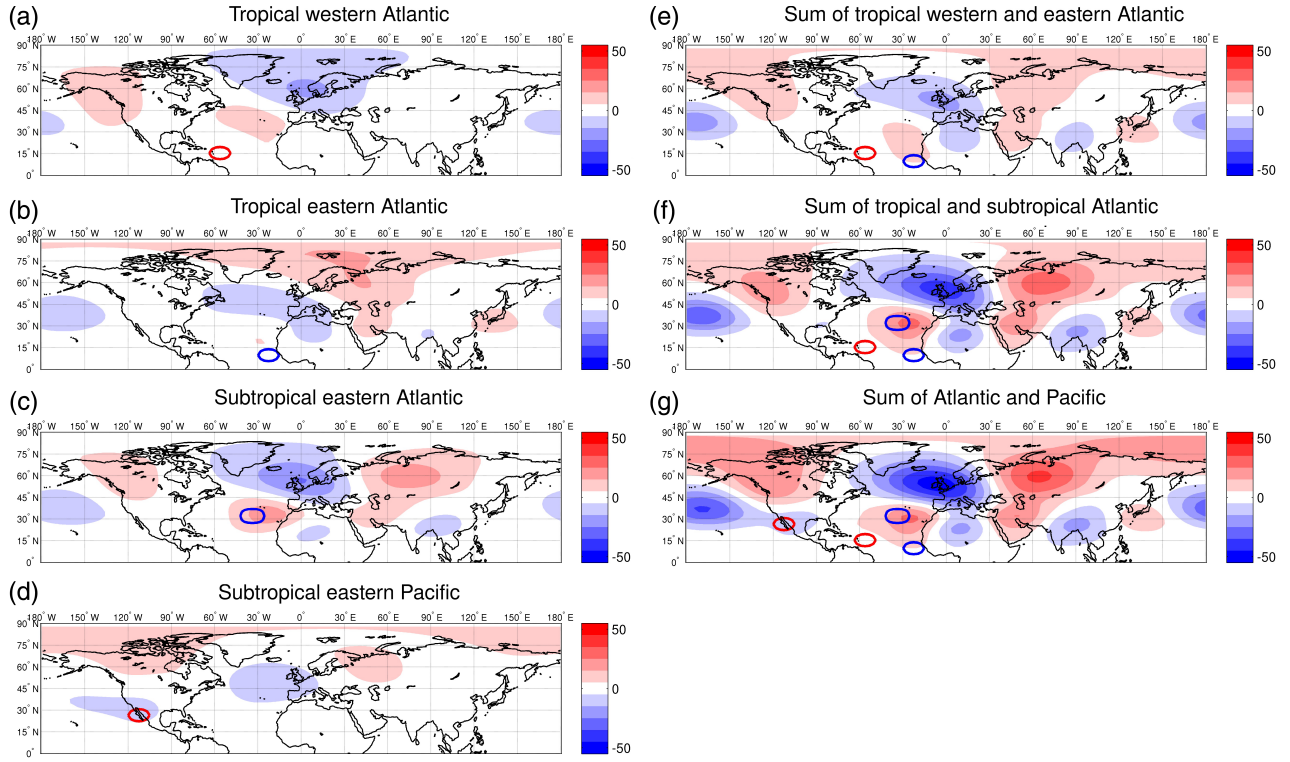

FIGURE 5 Barotropic model responses from selected individual RWS patches. Colour shading shows the 250 hPa geopotential height response (m) from the barotropic experiment, using patches in (a) tropical western Atlantic with amplitude 8×10^{-11} s^{-2}, (b) tropical eastern Atlantic with amplitude -8×10^{-11} s^{-2}, (c) subtropical eastern Atlantic with amplitude -16×10^{-11} s^{-2}, (d) subtropical eastern Pacific with amplitude 8×10^{-11} s^{-2}. (e) shows the sum of (a, b), (f) the sum of (a, b, c), and (g) the sum of (a, b, c, d). Vorticity forcings are shown as solid contours at $\pm2\times10^{-11}$ s^{-2}, with positive in red and negative in blue

patterns to those observed. While the $k2$ and $k3$ waves produced by the tropical eastern Atlantic patch (Figures 6e,f) are more different from the observed, this is consistent with the earlier finding that the tropical eastern Atlantic patch should not be considered alone, but when combined with the tropical western Atlantic patch gives a response (Figure 5e) more similar to the observation than from each patch individually. Finally, while the subtropical eastern Pacific patch produces a $k2$ wave (Figure 6i) that is similar to the observed, it produces a $k3$ wave (Figure 6j) with a phase more different from the observed. To summarize, barotropic experiments suggest regions – mainly in the tropical and subtropical Atlantic, and to a lesser extent the subtropical Pacific – force Rossby waves that can contribute to European precipitation events, and the $k2$ and $k3$ components seem particularly important. This indicates potential for forcing from these regions in both the barotropic model and in the observations, even though the model is also sensitive to forcing in other regions.

5 | RAY TRACING

To further investigate these teleconnections as Rossby waves, we perform ray tracing for the four forcing locations from the barotropic model section. Rays traced from the tropical western Atlantic (Figure 7a,b) can propagate across Europe for both $k2$ and $k3$, although the propagation is less robust for the $k2$ ensemble. Rays traced from the tropical eastern Atlantic can propagate across Europe robustly for $k2$ (Figure 7c). Rays traced from the subtropical eastern Atlantic can propagate across Europe robustly for both $k2$ and $k3$ (Figure 7e,f). These are in agreement with the barotropic model $k2$ and $k3$ responses resembling the observations, and suggest that the observed pattern can be explained by stationary long-wavelength Rossby waves forced from these regions.

The $k3$ ray traced from the tropical eastern Atlantic cannot propagate across Europe (Figure 7d), and this result is robust across all starting locations. This may be consistent with the aforementioned phase difference in the barotropic $k3$ response compared to the observed, and suggests that $k3$ wave propagation from this region cannot robustly propagate. Finally, all rays traced from the subtropical eastern Pacific do not reach Europe (Figure 7g,h), suggesting that the Pacific forcing teleconnection to Europe is not as important as the Atlantic forcings, again consistent with our barotropic model experiments which emphasize the role of the tropical Atlantic.

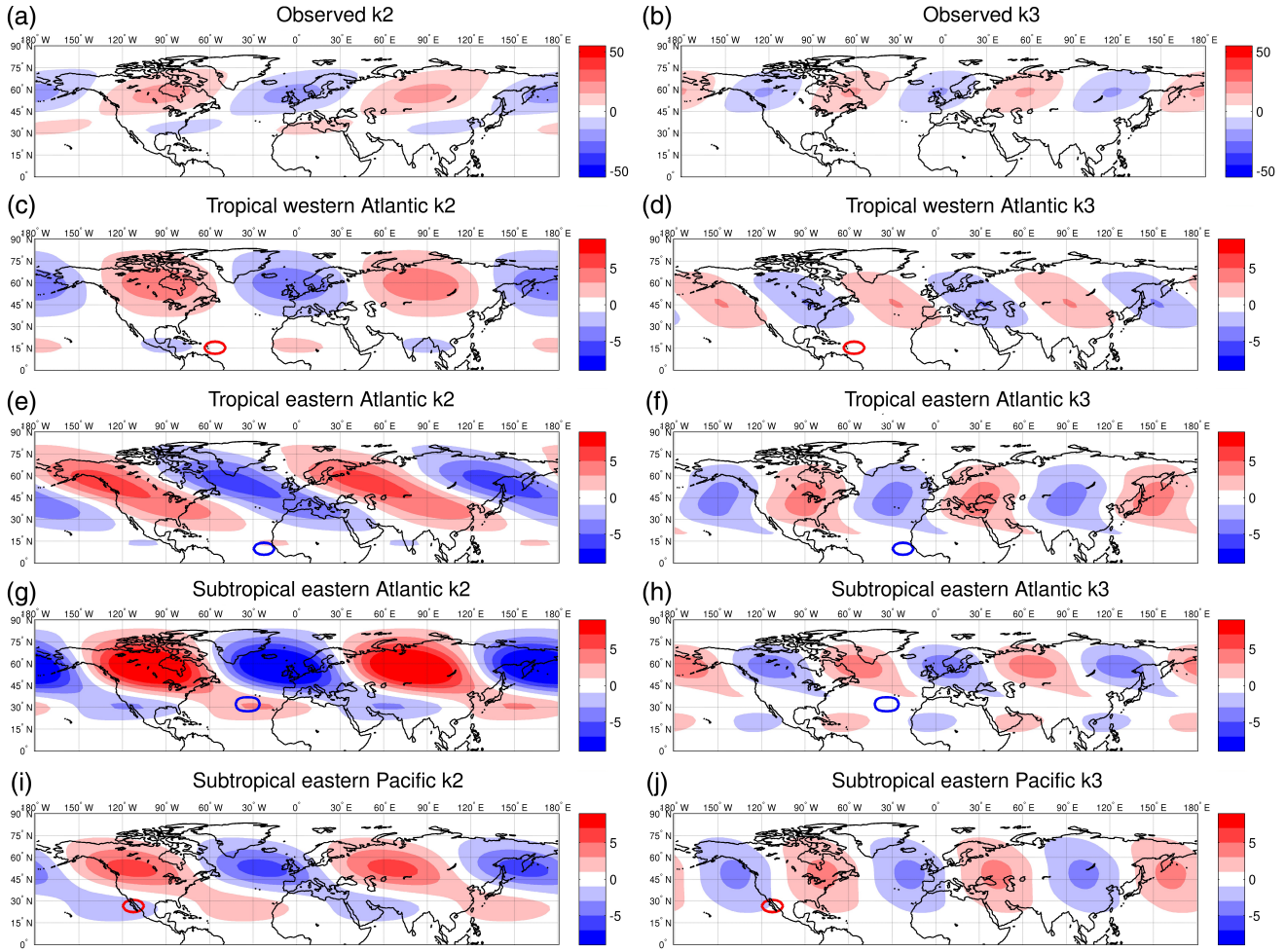

FIGURE 6 Fourier analysis of the barotropic model responses from selected Rossby wave source patches. Colour shadings show the zonal wavenumbers 2 and 3 components of 250 hPa geopotential height (m), of (a, b) the observed pattern, and barotropic model responses to patches at (c, d) tropical western Atlantic, (e, f) tropical eastern Atlantic (g, h) subtropical eastern Atlantic and (i, j) subtropical eastern Pacific. Vorticity forcings are shown as solid contour at $\pm 2 \times 10^{-11}$ s^{-2}, with positive in red and negative in blue. Note the different colour scales for observation and model

6 | BAROCLINIC MODEL EXPERIMENTS

In this section, we present baroclinic model responses to tropical heating. Following from our conclusion with the barotropic model, we first focus on the tropical Atlantic as a potential atmospheric driver of European precipitation events. From the heating coincidental with the European precipitation events (Figure 2f), we start by isolating the region of cooling in the tropical Atlantic just north of the Equator associated with reduced precipitation, to match the prominent region in the observed forcing. We use the radiative–convective equilibrium approximation to convert the cooling amplitude from around -20 W·m^{-2} in the observation to -0.17 K·day^{-1} in the model. However, the height response to this cooling is about ten times weaker than observed. This may be because we have only included one small region of forcing. There are also horizontal differences between the total observed forcing and our single idealised forcing. We therefore present results where the model cooling is ten times stronger than the observed cooling. Figure 8a shows the response in 250 hPa geopotential height to this idealised elliptical cooling in the model. A wave propagates into the North Atlantic and shows some similarity to that observed, with reduced height near the UK, increased height near northwestern Russia, reduced height near the south of the Aleutian Islands and increased height near northern North America. However, it is far from an exact match, with especially the wave response in the subtropical and central North Atlantic is not seen in the observation. Still, this idealised tropical Atlantic forcing experiment already shows promising results.

Whereas the RWS in the barotropic model is specified, the baroclinic model generates the RWS from the cooling. Figure 8b shows the RWS response calculated from

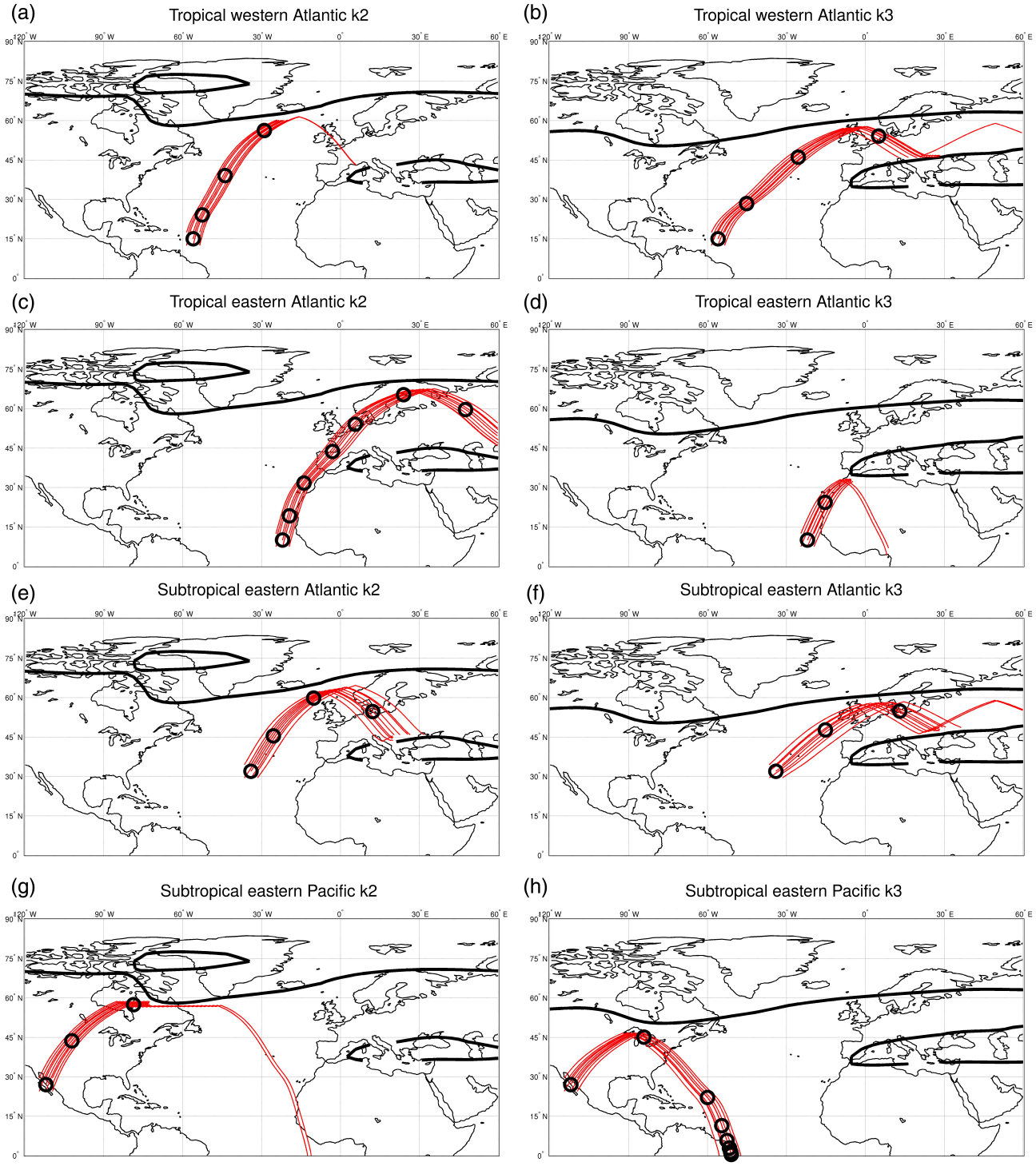

FIGURE 7 Ray tracing from the Atlantic and the Pacific. Ray tracing on 250 hPa climatological winds for zonal wavenumbers (a, c, e, g) 2 and (b, d, f, h) 3, initiated from (a, b) tropical western Atlantic, (c, d) tropical eastern Atlantic, (e, f) subtropical eastern Atlantic and (g, h) subtropical eastern Pacific. For each wavenumber traced, the corresponding stationary wavenumber contour is in black. Each ensemble ray is in red, and black circles are superimposed daily on the central ray

the zonal and meridional wind responses. A meridionally banded structure in RWS between 60°W and 30°W, with positive source along 15°N and negative source along 7°N, is prominent in the tropical Atlantic. This dipole agrees well with the observed RWS dipole in this region in Figure 2c. In addition, the two same-sign forcing regions in the tropical Atlantic from the barotropic model patch experiment (Figure 4f) are also included in this dipole, namely the positive source in the tropical western Atlantic and the negative source in the tropical eastern

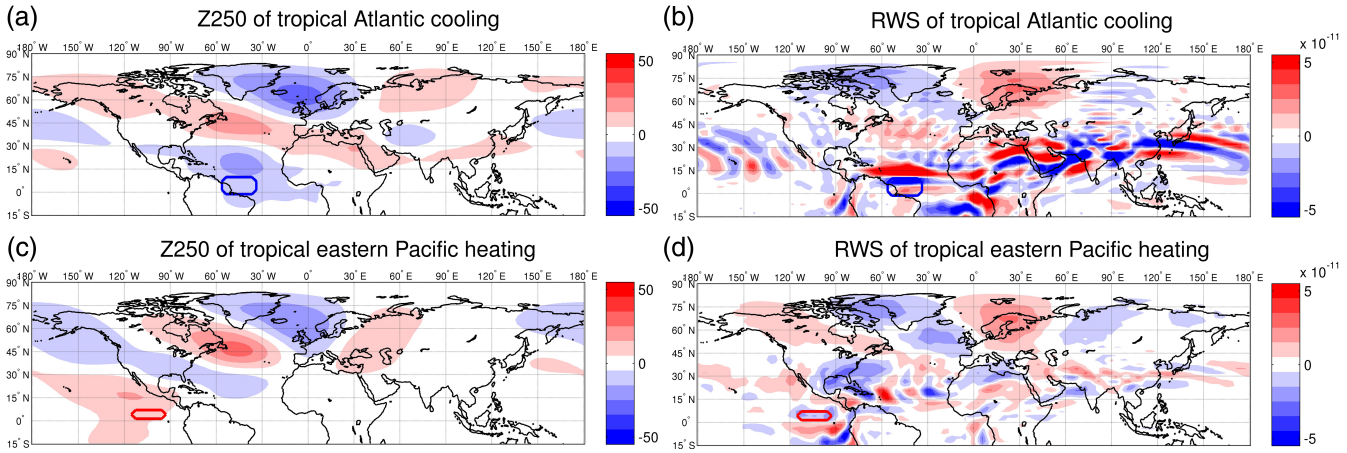

FIGURE 8 Baroclinic model responses to selected tropical cooling and heating. Colour shadings show the baroclinic experiment responses in 250 hPa (a, c) geopotential height (m) and (b, d) Rossby wave source (s^{-2}). Solid contours show the tropical forcing, with red for heating and blue for cooling

Atlantic. When looking at the individual patches in the barotropic experiments, we have shown that combining both of these sources together give a more similar wave pattern (Figure 5e) to the observed than from each source individually (Figures 5a,b). This agrees with our baroclinic model result, which suggests that both of these sources are generated together from the same region of cooling.

The RWS shows some small-scale ripple-like structures, for example near 30°N, 90°E. We suspect these to be associated with the nearby orographic features, namely the Himalayas in northern India. These RWS ripples seen in our responses could be artefacts of our model, since we have applied a very strong constraint on the inverse initial tendency. However, these should not affect our RWS conclusions in the baroclinic experiments, which are far away from high orography.

We also perform an experiment using the region of heating just south of the Equator. As this heating is close to the previous region of cooling and is opposite in sign, the response is a similar wave but with the opposite sign (not shown). However, the two waves do not cancel out completely, especially the low over the UK and Iceland, because the region of heating is narrower meridionally and also has a weaker amplitude on average spatially. To summarize, results from the idealised cooling in the tropical Atlantic agree with some of the main regions of RWS in the tropical Atlantic from observations and from the barotropic model patch experiment.

Next, we look into the Subtropics. The same-sign forcing region identified in the subtropical eastern Atlantic near 30°W, 30°N in Figure 4f is not present in the baroclinic model RWS, although there is a similarly negative RWS just to the southwest of this region. A possible reason is that this observed negative region is a consequence of the wave itself, since it is in the Subtropics and close to the Extratropics.

In the Pacific, there is another prominent region of subtropical RWS in the Gulf of California in Figure 4f, and Figure 2d shows a strengthened ITCZ in the tropical eastern Pacific. When heating is applied in this region, the geopotential height response (Figure 8c) matches partly with the observation over the UK and western Russia. In the vicinity of the heating, positive RWS is generated over the Gulf of California (Figure 8d), which matches with both the observation and with the result from the same-sign barotropic model patch experiments. Therefore this suggests that, in addition to the cooling in the tropical Atlantic, heating anomalies in the tropical eastern Pacific may also contribute to the observed pattern during European precipitation events, but the contribution to the lower heights near the UK is weaker from the Pacific than from the Atlantic.

7 | CONCLUSIONS AND DISCUSSION

From observations, we have identified a wave-like pattern associated with seasonal northwestern European precipitation events. It shows qualitative linearity with respect to the dry and wet events. It is associated with tropical precipitation anomalies, which prompted us to investigate if there is a tropical–extratropical teleconnection. Our barotropic model patch experiments isolate several regions of the observed Rossby wave source, some of which are also statistically significant, which can force a wave similar to that observed. These regions include the tropical western and eastern Atlantic, the subtropical eastern Atlantic and,

to a smaller degree, the subtropical eastern Pacific. Zonal wavenumber 2 and 3 components of the barotropic model responses match well with observations and ray tracing also supports the importance of these components.

Following up on these source regions, baroclinic model experiments show that the observed cooling associated with reduced precipitation in the tropical Atlantic can generate some of the observed Rossby wave sources in the tropical Atlantic. The observed heating associated with increased precipitation in the tropical eastern Pacific can generate the observed Rossby wave source at the Gulf of California. There may be a link between the simultaneous reduced precipitation in the tropical Atlantic and the increased precipitation in the tropical eastern Pacific, as shown by the regression coefficients of opposite signs in both regions in the observed precipitation (Figure 2d).

While Scaife *et al.* (2019) found significant inter-basin precipitation connections in observations to be due to ENSO, the correlation between our European precipitation time series and the ENSO index is only 0.18 and is insignificant at 95% confidence, indicating ENSO has little association with our events. Instead, our tropical precipitation anomalies resemble more those associated with the NAO (not shown), consistent with the NAO index correlating at –0.44 with our European precipitation time series. Closer analysis of individual years reveals that about 60% of our European wet and dry events were significantly influenced by our tropical precipitation anomalies. While our results show more connection to the NAO than to ENSO, the NAO cannot capture the majority of the variability. Occasional strong ENSO events can also lead to European wet and dry events through forcings and mechanisms which are different from ours.

Dunstone *et al.* (2018) studied the 2016–2017 winter, which was one of the driest on record for Europe (Figure 1a). They found results for this dry year very similar to our European dry events. Not only were the heights similar in the North Atlantic–European region, they also found a dipole in tropical precipitation over the equatorial Atlantic indicating a northward shift of the ITCZ (Dunstone *et al.*, 2018, their figure 5e). The RWS also showed a dipole structure in the tropical Atlantic, with negative anomalies near 15°N and positive anomalies just south of it (Dunstone *et al.*, 2018, their figure 5f). They also compared 2016–2017 with 1994–1995 where Europe had its wettest winter (Figure 1a). The 1994–1995 anomalies in heights, in tropical Atlantic precipitation and in tropical Atlantic RWSs were opposite in sign to the 2016–2017 winter (Dunstone *et al.*, 2018, their figure 4), and also in agreement with the results of our wet events. Another recent wet winter for the UK of 2013–2014 also showed tropical Atlantic RWS anomalies similar to 1994–1995 and opposite in sign to 2016–2017 (Knight *et al.*, 2017, their figure 4). They suggested increased Amazonian precipitation could be a Rossby wave driver for that winter. While the winter of 2013–2014 does not show significant precipitation over our northwestern European box in our recent GPCP index (Figure 1a), our longer CRU index shows increased Amazonian precipitation (Figure 1b), although not statistically significant.

Rossby wave propagation is affected by both the forcing and the basic state on which it propagates. So far, we have looked only at the effect of anomalous tropical forcings. However, the basic state is also important because the zonal winds affect the waveguides (Hoskins and Karoly, 1981). Associated with our European precipitation events is a North Atlantic jet shift (Figure 2b). However, we find only subtle differences in the waveguides and the rays traced, when including the regressed wind anomalies in the basic state (not shown). We therefore conclude that the basic state anomalies are less important than the tropical forcing anomalies during these European precipitation events.

Finally, while we have focused on the tropical forcing, extratropical forcing may also play a role in the extratropical Rossby wave during our European precipitation events. Using a model that can treat thermal forcing and transient eddy forcing separately, Jung *et al.* (2017) showed that temperature anomalies in the western North Atlantic Ocean alter the transient eddy vorticity flux, which then acts as a source for a Rossby wave propagating to the Barents–Kara Seas. In this study, we have not investigated any possible contributions from the large baroclinic eddy activities in the North Atlantic.

To conclude, we have identified potential forcing regions in the Tropics during northwestern European precipitation events, which are consistent between the observation and our models. We suggest that reduced precipitation in the tropical Atlantic, and to a smaller degree increased precipitation in the tropical eastern Pacific, can drive Rossby waves into the North Atlantic and contribute to the dynamics observed in these European precipitation events. Our results may also be applied to European drought events, because of the qualitative linearity in the observations and in our linear methods. Our idealised models have proved useful for testing potential mechanisms, but further work is needed to investigate the role of these forcing regions in more complex models, including those with interactive ocean and land components.

ACKNOWLEDGEMENTS

We acknowledge the Dynamical Processes Research Group at the University of Reading for providing the baroclinic model. We acknowledge Matthew Patterson for providing the heating data. This study was

funded by the NERC IMPETUS project (NE/L01047X/1). CO was funded by the NERC SummerTIME project (NE/M005887/1). AAS was supported by the joint UK BEIS/Defra Met Office Hadley Centre Climate Programme (GA01101). The research materials supporting this publication can be accessed by contacting ronald.li@physics.ox.ac.uk. We thank the two anonymous reviewers who provided valuable comments that significantly improved our manuscript.

ORCID

Ronald K. K. Li https://orcid.org/0000-0001-9091-628X
Tim Woollings https://orcid.org/0000-0002-5815-9079
Chris O'Reilly https://orcid.org/0000-0002-8630-1650

REFERENCES

Adler, R.F., Huffman, G.J., Chang, A., Ferraro, R., Xie, P.-P., Janowiak, J., Rudolf, B., Schneider, U., Curtis, S., Bolvin, D., Gruber, A., Susskind, J., Arkin, P. and Nelkin, E. (2003) The version-2 global precipitation climatology project (GPCP) monthly precipitation analysis (1979-present). *Journal of Hydrometeorology*, 4, 1147–1167. https://doi.org/10.1175/1525-7541(2003)004<1147:TVGPCP>2.0.CO;2

Anstey, J.A. and Shepherd, T.G. (2014) High-latitude influence of the quasi-biennial oscillation. *Quarterly Journal of the Royal Meteorological Society*, 140, 1–21. https://doi.org/10.1002/qj.2132

Ayarzagüena, B., Ineson, S., Dunstone, N.J., Baldwin, M.P. and Scaife, A.A. (2018) Intraseasonal effects of El Niño Southern Oscillation on North Atlantic climate. *Journal of Climate*, 31, 8861–8873. https://doi.org/10.1175/JCLI-D-18-0097.1

Barsugli, J.J. and Sardeshmukh, P.D. (2002) Global atmospheric sensitivity to tropical SST anomalies throughout the Indo-Pacific basin. *Journal of Climate*, 15, 3427–3442. https://doi.org/10.1175/1520-0442(2002)015<3427:GASTTS>2.0.CO;2

Branstator, G. (1995) Organization of storm track anomalies by recurring low-frequency circulation anomalies. *Journal of the Atmospheric Sciences*, 52, 207–226. https://doi.org/10.1175/1520-0469(1995)052<0207:OOSTAB>2.0.CO;2

Davies, H.C. (2015) Weather chains during the 2013/2014 winter and their significance for seasonal prediction. *Nature Geoscience*, 8, 833–837. https://doi.org/10.1038/ngeo2561

Davini, P., von Hardenberg, J. and Corti, S. (2015) Tropical origin for the impacts of the Atlantic multidecadal variability on the Euro-Atlantic climate. *Environmental Research Letters*, 10(094010). https://doi.org/10.1088/1748-9326/10/9/094010

Dee, D.P., Uppala, S.M., Simmons, A.J., Berrisford, P., Poli, P., Kobayashi, S., Andrae, U., Balmaseda, M.A., Balsamo, G., Bauer, P., Bechtold, P., Beljaars, A.C.M., van de Berg, L., Bidlot, J., Bormann, N., Delsol, C., Dragani, R., Fuentes, M., Geer, A.J., Haimberger, L., Healy, S.B., Hersbach, H., Hólm, E.V., Isaksen, L., Kållberg, P., Köhler, M., Matricardi, M., McNally, A.P., Monge-Sanz, B.M., Morcrette, J.-J., Park, B.-K., Peubey, C., de Rosnay, P., Tavolato, C., Thépaut, J.-N. and Vitart, F. (2011) The ERA-Interim reanalysis: configuration and performance of the data assimilation system. *Quarterly Journal of the Royal Meteorological Society*, 137, 553–597. https://doi.org/10.1002/qj.828

Dunstone, N., Scaife, A.A., MacLachlan, C., Knight, J., Ineson, S., Smith, D., Thornton, H., Gordon, M., McLean, P., Palin, E., Hardiman, S. and Walker, B. (2018) Predictability of European winter 2016/2017. *Atmospheric Science Letters*, 19(12). https://doi.org/10.1002/asl.868

Feldstein, S.B. (2003) The dynamics of NAO teleconnection pattern growth and decay. *Quarterly Journal of the Royal Meteorological Society*, 129, 901–924. https://doi.org/10.1256/qj.02.76

Folland, C.K., Palmer, T.N. and Parker, D.E. (1986) Sahel rainfall and worldwide sea temperatures, 1901–85. *Nature*, 320, 602–607. https://doi.org/10.1038/320602a0

Hannachi, A., Jolliffe, I.T. and Stephenson, D.B. (2007) Empirical orthogonal functions and related techniques in atmospheric science: A review. *International Journal of Climatology*, 27, 1119–1152. https://doi.org/10.1002/joc.1499

Hardiman, S.C., Dunstone, N.J., Scaife, A.A., Smith, D.M., Ineson, S., Lim, J. and Fereday, D. (2019) The impact of strong El Niño and La Niña events on the North Atlantic. *Geophysical Research Letters*, 46, 2874–2883. https://doi.org/10.1029/2018GL081776

Harris, I., Jones, P., Osborn, T. and Lister, D. (2014) Updated high-resolution grids of monthly climatic observations – the CRU TS3.10 dataset. *International Journal of Climatology*, 34, 623–642. https://doi.org/10.1002/joc.3711

Hoskins, B.J. and Ambrizzi, T. (1993) Rossby wave propagation on a realistic longitudinally varying flow. *Journal of the Atmospheric Sciences*, 50, 1661–1671. https://doi.org/10.1175/1520-0469(1993)050<1661:RWPOAR>2.0.CO;2

Hoskins, B.J. and Karoly, D.J. (1981) The steady linear response of a spherical atmosphere to thermal and orographic forcing. *Journal of the Atmospheric Sciences*, 38, 1179–1196. https://doi.org/10.1175/1520-0469(1981)038<1179:TSLROA>2.0.CO;2

Hoskins, B.J. and Simmons, A.J. (1975) A multi-layer spectral model and the semi-implicit method. *Quarterly Journal of the Royal Meteorological Society*, 101, 637–655. https://doi.org/10.1002/qj.49710142918

Huntingford, C., Marsh, T., Scaife, A.A., Kendon, E.J., Hannaford, J., Kay, A.L., Lockwood, M., Prudhomme, C., Reynard, N.S., Parry, S., Lowe, J.A., Screen, J.A., Ward, H.C., Roberts, M., Stott, P.A., Bell, V.A., Bailey, M., Jenkins, A., Legg, T., Otto, F.E.L., Massey, N., Schaller, N., Slingo, J. and Allen, M.R. (2014) Potential influences on the United Kingdom's floods of winter 2013/14. *Nature Climate Change*, 4, 769–777. https://doi.org/10.1038/nclimate2314

Jin, F. and Hoskins, B.J. (1995) The direct response to tropical heating in a baroclinic atmosphere. *Journal of the Atmospheric Sciences*, 52, 307–319. https://doi.org/10.1175/1520-0469(1995)052<0307:TDRTTH>2.0.CO;2

Jung, O., Sung, M.-K., Sato, K., Lim, Y.-K., Kim, S.-J., Baek, E.-H., Jeong, J.-H. and Kim, B.-M. (2017) How does the SST variability over the western North Atlantic Ocean control Arctic warming over the Barents–Kara Seas?. *Environmental Research Letters*, 12(034021). https://doi.org/10.1088/1748-9326/aa5f3b

Kanamitsu, M., Ebisuzaki, W., Woollen, J., Yang, S.-K., Hnilo, J.J., Fiorino, M. and Potter, G.L. (2002) NCEP-DOE AMIP-II Reanalysis (R-2). *Bulletin of the American Meteorological Society*, 83, 1631–1644. https://doi.org/10.1175/BAMS-83-11-1631

Knight, J.R., Maidens, A., Watson, P.A.G., Andrews, M., Belcher, S., Brunet, G., Fereday, D., Folland, C.K., Scaife, A.A. and Slingo, J. (2017) Global meteorological influences on the record UK rainfall of winter 2013–14. *Environmental Research Letters*, 12(074001). https://doi.org/10.1088/1748-9326/aa693c

Lamb, P.J. (1978) Large-scale tropical Atlantic surface circulation patterns associated with Subsaharan weather anomalies. *Tellus*, 30, 240–251. https://doi.org/10.3402/tellusa.v30i3.10338

Li, C. and Wettstein, J.J. (2012) Thermally driven and eddy-driven jet variability in reanalysis. *Journal of Climate*, 25, 1587–1596. https://doi.org/10.1175/JCLI-D-11-00145.1

Liu, Y., Hoskins, B.J. and Blackburn, M. (2007) Impact of Tibetan orography and heating on the summer flow over Asia. *Journal of the Meteorological Society of Japan. Series II*, 85B, 1–19

Manola, I., Haarsma, R.J. and Hazeleger, W. (2013) Drivers of North Atlantic Oscillation events. *Tellus A: Dynamic Meteorology and Oceanography*, 65(19741). https://doi.org/10.3402/tellusa.v65i0.19741

Matthews, A.J., Hoskins, B.J. and Masutani, M. (2004) The global response to tropical heating in the Madden–Julian Oscillation during the northern winter. *Quarterly Journal of the Royal Meteorological Society*, 130, 1991–2011. https://doi.org/10.1256/qj.02.123

O'Reilly, C.H., Weisheimer, A., Woollings, T., Gray, L.J. and MacLeod, D. (2019) The importance of stratospheric initial conditions for winter North Atlantic Oscillation predictability and implications for the signal-to-noise paradox. *Quarterly Journal of the Royal Meteorological Society*, 145, 131–146. https://doi.org/10.1002/qj.3413

O'Reilly, C.H., Woollings, T., Zanna, L. and Weisheimer, A. (2018) The impact of tropical precipitation on summertime Euro-Atlantic Circulation via a circumglobal wave train. *Journal of Climate*, 31, 6481–6504. https://doi.org/10.1175/JCLI-D-17-0451.1

Poli, P., Hersbach, H., Dee, D.P., Berrisford, P., Simmons, A.J., Vitart, F., Laloyaux, P., Tan, D.G.H., Peubey, C., Thépaut, J.-N., Trémolet, Y., Hólm, E.V., Bonavita, M., Isaksen, L. and Fisher, M. (2016) ERA-20C: an atmospheric reanalysis of the Twentieth Century. *Journal of Climate*, 29, 4083–4097. https://doi.org/10.1175/JCLI-D-15-0556.1

Röthlisberger, M., Frossard, L., Bosart, L.F., Keyser, D. and Martius, O. (2019) Recurrent synoptic-scale Rossby wave patterns and their effect on the persistence of cold and hot spells. *Journal of Climate*, 32, 3207–3226. https://doi.org/10.1175/JCLI-D-18-0664.1

Sardeshmukh, P.D. and Hoskins, B.J. (1988) The generation of global rotational flow by steady idealised tropical divergence. *Journal of Atmospheric Sciences*, 45, 1228–1251

Scaife, A.A., Arribas, A., Blockley, E., Brookshaw, A., Clark, R.T., Dunstone, N., Eade, R., Fereday, D., Folland, C.K., Gordon, M., Hermanson, L., Knight, J.R., Lea, D.J., MacLachlan, C., Maidens, A., Martin, M., Peterson, A.K., Smith, D., Vellinga, M., Wallace, E., Waters, J. and Williams, A. (2014a) Skilful long-range prediction of European and North American winters. *Geophysical Research Letters*, 41, 2514–2519. https://doi.org/10.1002/2014GL059637

Scaife, A.A., Athanassiadou, M., Andrews, M., Arribas, A., Baldwin, M., Dunstone, N., Knight, J., MacLachlan, C., Manzini, E., Müller, W.A., Pohlmann, H., Smith, D., Stockdale, T. and Williams, A. (2014b) Predictability of the Quasi-Biennial Oscillation and its northern winter teleconnection on seasonal to decadal timescales. *Geophysical Research Letters*, 41, 1752–1758. https://doi.org/10.1002/2013GL059160

Scaife, A.A., Comer, R., Dunstone, N., Fereday, D., Folland, C.K., Good, E., Gordon, M., Hermanson, L., Ineson, S., Karpechko, A., Knight, J., MacLachlan, C., Maidens, A., Peterson, K.A., Smith, D., Slingo, J. and Walker, B. (2017a) Predictability of European winter 2015/2016. *Atmospheric Science Letters*, 18, 38–44. https://doi.org/10.1002/asl.721

Scaife, A.A., Comer, R.E., Dunstone, N.J., Knight, J.R., Smith, D.M., MacLachlan, C., Martin, N., Peterson, K.A., Rowlands, D., Carroll, E.B., Belcher, S. and Slingo, J. (2017b) Tropical rainfall, Rossby waves and regional winter climate predictions. *Quarterly Journal of the Royal Meteorological Society*, 143, 1–11. https://doi.org/10.1002/qj.2910

Scaife, A.A., Ferranti, L., Alves, O., Athanasiadis, P., Baehr, J., Dequé, M., Dippe, T., Dunstone, N., Fereday, D., Gudgel, R.G., Greatbatch, R.J., Hermanson, L., Imada, Y., Jain, S., Kumar, A., MacLachlan, C., Merryfield, W., Müller, W.A., Ren, H.-L., Smith, D., Takaya, Y., Vecchi, G. and Yang, X. (2019) Tropical rainfall predictions from multiple seasonal forecast systems. *International Journal of Climatology*, 39, 974–988. https://doi.org/10.1002/joc.5855

Schneider, U., Ziese, M., Meyer-Christoffer, A., Finger, P., Rustemeier, E. and Becker, A. (2016) The new portfolio of global precipitation data products of the Global Precipitation Climatology Centre suitable to assess and quantify the global water cycle and resources. *Proceedings of the International Association of Hydrological Sciences*, 374, 29–34. https://doi.org/10.5194/piahs-374-29-2016

Smith, D.M., Scaife, A.A., Eade, R. and Knight, J.R. (2016) Seasonal to decadal prediction of the winter North Atlantic Oscillation: emerging capability and future prospects. *Quarterly Journal of the Royal Meteorological Society*, 142, 611–617. https://doi.org/10.1002/qj.2479

Sun, Q., Miao, C., Duan, Q., Ashouri, H., Sorooshian, S. and Hsu, K.-L. (2018) A review of global precipitation data sets: data sources, estimation and intercomparisons. *Reviews of Geophysics*, 56, 79–107. https://doi.org/10.1002/2017RG000574

Wilks, D.S. (2016) "The stippling shows statistically significant grid points": how research results are routinely overstated and overinterpreted, and what to do about it. *Bulletin of the American Meteorological Society*, 97, 2263–2273. https://doi.org/10.1175/BAMS-D-15-00267.1

Xie, P. and Arkin, P.A. (1997) Global precipitation: a 17-year monthly analysis based on gauge observations, satellite estimates, and numerical model outputs. *Bulletin of the American Meteorological Society*, 78, 2539–2558. https://doi.org/10.1175/1520-0477(1997)078<2539:GPAYMA>2.0.CO;2

How to cite this article: Li RKK, Woollings T, O'Reilly C, Scaife AA. Tropical atmospheric drivers of wintertime European precipitation events. *QJR Meteorol Soc*. 2020;1–15.
https://doi.org/10.1002/qj.3708